Compact Optical Atomic Clock Based on a Two-Photon Transition in Rubidium

Kyle W. Martin,[1] Gretchen Phelps,[2] Nathan D. Lemke,[2] Matthew S. Bigelow,[1] Benjamin Stuhl,[3] Michael Wojcik,[3] Michael Holt,[3] Ian Coddington,[4] Michael W. Bishop,[2] and John H. Burke[2]

[1]*Applied Technology Associates d/b/a ATA, 1300 Britt Street, Southeast Albuquerque, New Mexico 87123, USA*

[2]*Air Force Research Laboratory, Space Vehicles Directorate, Kirtland Air Force Base, New Mexico 87117, USA*

[3]*Space Dynamics Laboratory, 1695 North Research Park Way, North Logan, Utah 84341, USA*

[4]*National Institute of Standards and Technology, 325 Broadway, Boulder, Colorado 80305, USA*

(Received 20 September 2017; revised manuscript received 28 November 2017; published 18 January 2018)

Extralaboratory atomic clocks are necessary for a wide array of applications (e.g., satellite-based navigation and communication). Building upon existing vapor-cell and laser technologies, we describe an optical atomic clock, designed around a simple and manufacturable architecture, that utilizes the 778-nm two-photon transition in rubidium and yields fractional-frequency instabilities of $4 \times 10^{-13}/\sqrt{\tau(s)}$ for τ from 1 to 10 000 s. We present a complete stability budget for this system and explore the required conditions under which a fractional-frequency instability of 1×10^{-15} can be maintained on long time scales. We provide a precise characterization of the leading sensitivities to external processes, including magnetic fields and fluctuations of the vapor-cell temperature and 778-nm laser power. The system is constructed primarily from commercially available components, an attractive feature from the standpoint of the commercialization and deployment of optical frequency standards.

DOI: 10.1103/PhysRevApplied.9.014019

I. INTRODUCTION

High-stability clocks and oscillators play an integral role in many modern technologies, such as navigation and communications [1]. Laboratory-based primary frequency standards, which utilize microwave transitions between atomic hyperfine levels, provide the highest degree of timing accuracy and are used to form international time scales [2–4]; in many cases, however, applications beyond timekeeping require clocks that are deployed outside the laboratory setting. One well-known case is that of global navigation satellite systems, which employ space-qualified frequency standards aboard satellites in medium earth orbit and/or geosynchronous orbit [1,5]. While portable clocks are typically outpaced by their laboratory counterparts in terms of stability and accuracy, they nonetheless offer very low levels of frequency instabilities; in the case of rubidium atomic frequency standards, clocks are commercially available with a fractional drift rate below 10^{-13}/day and a fractional-frequency noise floor of less than 10^{-14} [6]. Moreover, these deployable microwave clocks are expected to benefit from recent demonstrations of compact frequency standards based on laser-pumped vapor cells [7–9] and cold atoms [10].

With the advent of fully stabilized optical frequency combs in 2000 [11–13], optical frequency standards have rapidly surpassed the capabilities of microwave clocks in both stability [14,15] and systematic uncertainty [16–18]. Efforts to reduce the size and increase the portability and autonomy of these systems form an active research area [19–24]. Of particular interest from the standpoint of deployable clocks is an optical frequency standard that can surpass existing commercial clocks by a factor of 10 in both short- and long-term stability, which translates to approximate Allan deviations of 1×10^{-13} at 1 s and 1×10^{-15} at 1 day, without significantly increased volume ($\lesssim$10 l) or power consumption ($\lesssim$20 W). However, a fully automated, portable, and compact optical atomic clock has yet to emerge. Much of the difficulty in developing compact and environmentally robust optical frequency standards lies with the complicated laser sources and optical systems required for laser cooling and interrogating an atomic sample. Moreover, given the high quality factor (i.e., narrow spectral linewidth) of typical optical clock transitions, laser prestabilization to a high-finesse Fabry-Perot cavity is generally required, which adds significant complexity and volume to the system. Finally, optical frequency combs have not, until recently, been sufficiently compact or robust to warrant an effort toward deployment of an optical clock.

With these challenges in mind, we investigate an optical clock based on a two-photon transition in a hot Rb vapor. Two-photon transitions are attractive because they enable Doppler-free spectra [25] without the need for laser cooling, provided that two antiparallel laser beams are used to

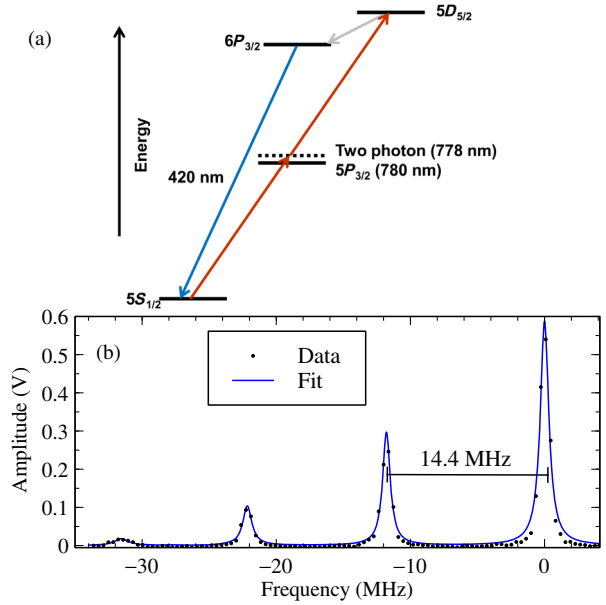

FIG. 1. (a) Partial energy-level diagram of Rb. The virtual state associated with two-photon excitation at 778 nm is shown by the dashed line. The cascade decay path $5D_{5/2} \rightarrow 6P_{3/2} \rightarrow 5S_{1/2}$ results in the emission of a 420-nm photon, which we use to observe the two-photon resonance. (b) Two-photon excitation spectrum of ^{87}Rb ($F = 2$). The frequency axis is presented as the 778-nm laser detuning from the $F = 2 \rightarrow F' = 4$ transition, which has the largest Clebsch-Gordan coefficient. Included is a fit using a sum of four Lorentzian peaks of equal width and with relative peak heights and detunings constrained by the values presented in Ref. [26]. The fitting procedure results in a full-width-at-half-maximum linewidth of 609 kHz, which exceeds the natural linewidth by a factor of 1.8, which, we expect, is due to line broadening from helium collisions [33].

interrogate the atomic vapor. Moreover, the two-photon transition can often be observed via a fluorescence signal that is spectrally resolvable from the probe laser; together with the large number of atoms interrogated in the vapor phase, this system enables a very high signal-to-noise measurement of the clock transition. For the case described here of the 778-nm two-photon transition in rubidium, fluorescence is readily observable at 420 nm, and stray light in the near infrared is rejected with standard optical filtering. We further benefit, in the case of the Rb $5S_{1/2} \rightarrow 5D_{5/2}$ transition from the nearby intermediate state $5P_{3/2}$ that is only separated by 2 nm, from the virtual two-photon state (see Fig. 1), facilitating significant atomic excitation rates at modest optical intensities [26–28]. Conveniently, 778.1-nm light can be produced by second-harmonic generation (SHG) of 1556.2 nm, which falls in the telecommunications *C* band, allowing the use of mature laser sources and erbium fiber frequency combs [23,24,29]. An additional feature of this system is the availability of commercial laser systems for which the fast linewidth is significantly below the natural linewidth of the excited clock state ($\Delta\nu \approx 330$ kHz, as observed at 778 nm), alleviating the requirement for laser prestabilization to a high-finesse optical cavity. These appealing features motivate our investigation of an optical rubidium atomic frequency standard as a future portable clock. Previous investigations into this transition were carried out in the 1990s [26–28], with some renewed interest recently leveraging the development of laser and frequency-comb technologies [30–32]. While the work presented here does not yet specifically represent a designed system for a small footprint and low power consumption, we anticipate that it should be possible. As a first step, however, it must be shown that a vapor-cell-based two-photon clock can meet the demanding timing requirements needed to enable the above applications.

Two-photon transitions are known to suffer from large ac Stark shifts imparted by the laser used to excite the atomic vapor. Additionally, alkali vapor cells are significantly affected by collisions with background particles, either from buffer gases in microwave clocks [34] or from other alkali atoms in the case of optical clocks [33]. These effects require precise measurement and control of the laser power and vapor-cell temperature, respectively, in order to minimize the associated clock instabilities. While initial experiments showed vapor-cell-based two-photon frequency standards to be capable of instabilities as low as $3 \times 10^{-13}/\sqrt{\tau}$ for τ values of 1–2000 s, on longer time scales, the instability increased [28], and instability below 1×10^{-14} has not been observed. Here, we extend the range of integration to longer time scales and demonstrate a corresponding reduction of long-term instability, approaching the level of 1×10^{-15}. Key to this level of performance is tight control over the vapor density [33] and laser power [28], both of which we describe in detail below, together with a full stability budget for the frequency standard. Additionally, we describe a mode of operation where the 1-s instability is reduced to approximately 1×10^{-13}, with further reductions expected from future design iterations.

This paper is organized as follows. Section II describes the design of the frequency standard and measurement system. Section III provides detailed analysis of the known contributors to clock instability, with particular emphasis placed on the clock-laser-induced ac Stark shift, the collisional effects, the Zeeman shifts, and the short-term stability limitations. The performance of the frequency standard is detailed in Sec. IV, and the paper concludes in Sec. V with a discussion of conceived upgrades to the two-photon frequency standard.

II. EXPERIMENTAL APPARATUS

The design shown in Fig. 2 begins with a 1556-nm diode laser system that produces 20 mW of narrow-band light, with a fast linewidth of ≤ 2 kHz. This laser acts as the local oscillator for the frequency standard. A small portion of the seed-laser output is sampled by a fiber splitter to form an optical beat note with a fiber frequency comb based upon the design in Ref. [24]. The fully self-referenced frequency

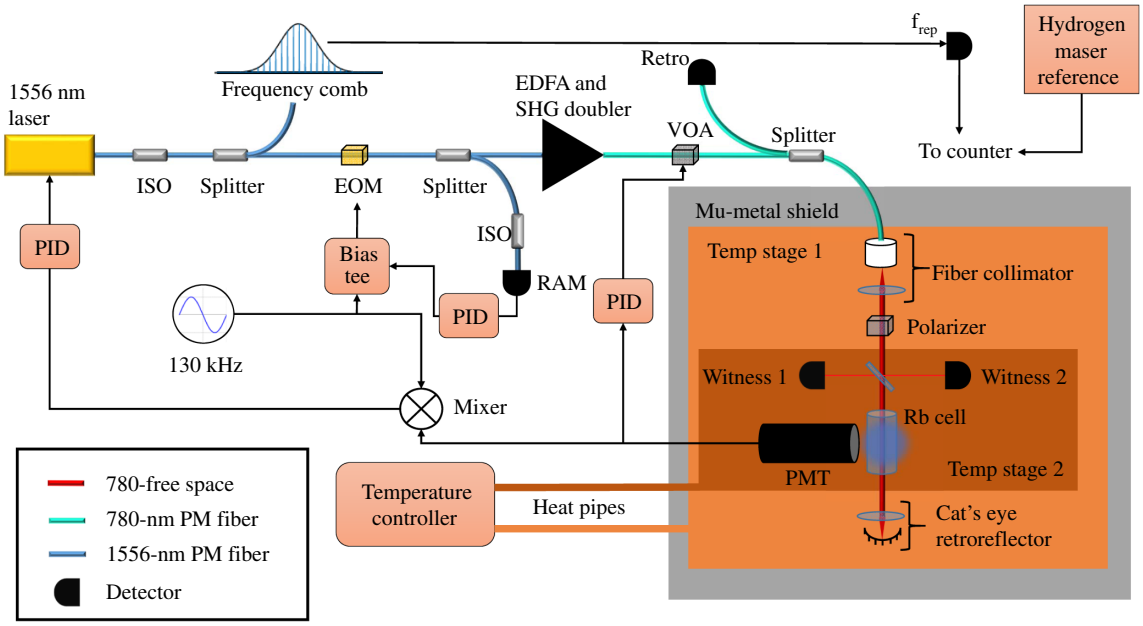

FIG. 2. An optical and simplified electrical schematic of the Rb two-photon frequency standard described in the text. EOM, electro-optic modulator; PMT, photomultiplier tube; VOA, variable optical attenuator; ISO, optical isolator; EDFA, erbium-doped fiber amplifier; SHG, second-harmonic generator; RAM, residual amplitude modulation; PID, proportional-integral-differential lock mechanism.

comb coherently divides the 192-THz optical waveform into about 200 MHz, which is the comb's pulse repetition rate. After stabilization of the optical beat-note and carrier-envelope offset frequency, the comb's repetition rate is photodetected, and a Microsemi 5125A, referenced to a hydrogen maser, is used as a frequency counter. The remaining portion of the 1556-nm laser output enters a fiber-coupled electro-optic modulator (EOM) formed in a proton-exchange waveguide embedded in lithium niobate, which is driven at 130 kHz. After the EOM, the light is amplified by an erbium-doped fiber amplifier and undergoes SHG in a periodically poled lithium niobate crystal, outputting as much as 1 W of 778.1-nm light. The output of the SHG crystal, typically around 100 mW, is subsequently sent through a variable optical attenuator (VOA), which is used for laser power stabilization, as described below. Typically, 30 mW of 778-nm light is delivered to the vapor-cell assembly.

The vapor-cell assembly is enclosed in a 5-mm-thick, single-layer mu-metal magnetic shield to reduce spectral broadening associated with the Zeeman shift. The vapor cell is heated to 100 °C to generate sufficient vapor density for a high-stability clock. To avoid local magnetic fields when heating the vapor cell, all heat is generated with resistive and thermoelectric devices located outside the magnetic shielding; water-filled heat pipes protrude through the magnetic shield and provide heat to the dual-zone temperature control stage surrounding the vapor cell. The vapor cell, which is a rectangular prism with dimensions $5 \times 5 \times 25$ mm, containing $> 99\%$ isotopically enriched ^{87}Rb, is placed such that it has a 1-K thermal gradient along its length, forcing the cell's cold spot on the pinched-off fill tube of the borosilicate glass cell. The vapor cell is oriented at Brewster's angle with respect to the incident laser beam to reduce stray reflections.

The 778-nm laser output is delivered by polarization-maintaining optical fiber through an opening in the magnetic shield, where it is collimated ($1/e^2$ intensity radius $w_0 = 0.66$ mm) using a nonmagnetic optical assembly. A calcite Glan-Taylor polarizer is placed at the output of the fiber launcher to reduce polarization wander. The laser beam is sampled by a glass plate pickoff before entering the vapor cell; Thorlabs SM05PD1A photodetectors, with dark current 20 nA and an active area of 3.5×3.5 mm, are placed on each side of the glass plate to monitor the optical power in the sampled beams. A cat's-eye retroreflector [35] provides a precisely anti-parallel reflected beam, which is necessary for eliminating Doppler broadening. A portion of the fluorescence at 420 nm passes through a short-pass optical filter and is detected by a photomultiplier tube (PMT) (dark current 5 nA). The PMT provides a fast temporal response and high electron-multiplying gain. After a transimpedance amplifier, the PMT output signal is demodulated by the 130-kHz sinusoidal modulation applied to the EOM in a phase detector, resulting in a laser-detuning-dependent error signal. A digital servo controller with dual integrators and approximately 50 kHz of bandwidth feeds the 1556-nm laser drive current to hold the laser on the two-photon resonance.

This design allows for the study of various parameters that contribute to the system's performance at different time scales. The short-term stability is determined by the atomic linewidth, the optical intensity, the detector collection efficiency, and the laser frequency-noise characteristics. The long-term stability, with a current goal of $<1\times10^{-15}$ for one day, requires the stabilization of various experimental and environmental parameters, including the vapor-cell temperature (the Rb vapor density), magnetic field, and optical power; these parameters are investigated in subsequent sections.

III. SOURCES OF CLOCK INSTABILITY

In this section, we discuss the leading sources of instability to the Rb two-photon system. Particular importance is given to rigorously determining the relevant sensitivity coefficients. Because our goals call for a stable frequency standard but not necessarily one with high accuracy, we do not undertake to precisely measure the magnitude of each systematic effect, but rather to characterize the stability requirements of external parameters such as the magnetic field and the laser power. Table I summarizes all of the clock shifts and environmental stability parameters necessary to achieve fractional-frequency instabilities of 1×10^{-15}.

A. Short-term stability

The practical noise limit of a frequency standard is the greater of the residual local oscillator (LO) noise and the shot noise associated with detection of the atomic transition. Continuously operated (as opposed to pulsed) frequency standards are most sensitive to LO noise at twice the modulation frequency ($f_m = 130$ kHz in this work) [36]. Noise at this frequency (or even higher harmonics) is down sampled by the demodulation process and remains partially uncompensated for, thereby degrading the frequency standard's stability in a manner that is analogous to the Dick effect in pulsed frequency standards [37]. This instability source is known as the intermodulation effect [36] and can be calculated as

$$\sigma_y^{(\mathrm{IM})}(\tau) = \frac{S_y^{(\mathrm{LO})}[2f_m]}{2\sqrt{\tau}}, \tag{1}$$

where $S_y^{(\mathrm{LO})}[2f_m]$ is the power spectral density of LO frequency noise at $2f_m$. Because we employ a low-noise (albeit free-running) 1556-nm diode laser as the local oscillator, the intermodulation effect is small and the associated white-noise frequency instability is estimated as $2.6\times10^{-14}/\sqrt{\tau}$. Under typical operating conditions, the frequency standard is limited not by this intermodulation process but rather by shot noise associated with fluorescence detection at 420 nm.

We can assess the expected instability by analyzing the voltage signal present at the output of the transimpedance amplifier that follows the PMT. Using a fast-Fourier-transform analyzer, we typically observe the signal's power spectral density (S_v) as white frequency noise between 1 and 100 kHz. Combined with knowledge of the detuning-dependent error-signal magnitude (V_e), the effective gain of the phase detector (g_{PD}) at the modulation frequency f_m, and the atomic linewidth $\Delta\nu$, we can estimate the clock instability as

$$\sigma_y(\tau) = \frac{\Delta\nu}{2\nu_0}\frac{g_{\mathrm{PD}}}{V_e}\sqrt{\frac{S_v}{\tau}}, \tag{2}$$

with τ being the integration time [28]. Typical values are shown in Table II and yield an expected 1-s Allan deviation of $\sigma_y(\tau=1\ \mathrm{s})\approx4.7\times10^{-13}$ for 30 mW of laser power incident on the vapor cell, which is close to the observed instability of $\sigma_y(\tau=1\ \mathrm{s})\approx4.1\times10^{-13}$ shown in Fig. 5. By varying the laser power and the resulting error-signal magnitude, we confirm that the frequency standard's performance is limited by shot noise on the PMT signal. However, we note that the calculated shot noise based on the mean PMT photocurrent is a factor of 2 smaller,

TABLE I. The environmental variables that impact ^{87}Rb clock performance are listed, along with the corresponding fractional-frequency sensitivity coefficient. The right column tabulates the stability requirement for each parameter to support a fractional-frequency instability of 1×10^{-15}.

Shift	Fractional coefficient	Stability at 1 day
778-nm ac Stark	4.8×10^{-13}/mW	2.1 μW
Rb density	1.1×10^{-12}/K	0.92 mK
Blackbody radiation	1.3×10^{-15}/K	770 mK
dc Stark	$5.9\times10^{-15}/(\mathrm{V/cm})^2$	0.17 $(\mathrm{V/cm})^2$
Second-order Doppler	1.0×10^{-15}/K	1.0 K
Zeeman	$6.5\times10^{-11}/\mathrm{G}^2$	3.9 mG
Helium collisional	2.7×10^{-8}/Torr	3.6×10^{-8} Torr

TABLE II. Typical parameters related to the short-term stability of the frequency standard as defined in the main text.

Parameter	Typical value
Detection rate	3.7×10^7/s
S_v	8.8×10^{-9} V^2/Hz
g_{PD}	0.41
V_e	0.065 V
$\Delta\nu$	608 kHz
Effective SNR (10-kHz bandwidth)	22
σ_y (1 s)	4.7×10^{-13}
$S_y^{(\mathrm{LO})}$ ($2f_m = 260$ kHz)	2.7×10^{-27}/Hz

indicating that the PMT has an effective noise factor of 3 dB, which is consistent with the description in Ref. [28].

In principle, the short-term instability of this system could be decreased by either collecting a greater fraction of the atomic fluorescence or increasing the laser power incident on the vapor cell. To demonstrate, we operate the frequency standard with significantly higher laser power, resulting in brighter fluorescence signals and reduced instabilities. The gray points in Fig. 5 demonstrate a 1-s Allan deviation of approximately 1×10^{-13}, which is consistent with the expected limit from our hydrogen-maser frequency reference. In-loop-stability estimates suggest that the actual 1-s Allan deviation for this mode of operation could be in the middle of the 10^{-14} decade; however, for the current design, operating at this level is detrimental to the long-term stability due to fluctuations of the ac Stark shift, as described in Sec. III B. To achieve the best long-term performance, we typically operate with 30 mW of laser power, as that represents a compromise between shot noise and the ac Stark shift.

B. ac Stark shift

Two-photon transitions are known to suffer from sizable ac Stark shifts associated with the probe laser [25]. The fractional ac Stark shift is given by

$$\frac{\Delta\nu}{\nu_0} = \frac{\Delta\alpha}{2c\epsilon_0 h}\overline{I(r)} = k(w_0)P, \tag{3}$$

where $\overline{I(r)} \propto P/w_0^2$ is the spatially averaged laser intensity, P is the one-way optical power incident on the vapor, $\nu_0 \approx 385$ THz is the two-photon laser frequency, w_0 is the $1/e^2$ intensity radius, $\Delta\alpha$ is the differential polarizability of the two clock states at 778.1 nm, and c, ϵ_0, and h are the speed of light, the permittivity of free space, and Planck's constant, respectively. We measure the shift experimentally utilizing the clock laser detailed in Fig. 2 together with an external Ti:sapphire laser. The role of the Ti:sapphire laser is to provide an additional light source whose ac Stark shift is characterized by varying its optical power, while the clock-laser system's properties are held constant. The Ti:sapphire laser is tuned slightly away from the two-photon resonance by 2.6 GHz to an optical frequency of 385 287.8 GHz. This optical frequency is selected because it is far enough detuned to induce no measurable excitation of the vapor, yet near enough to the two-photon resonance to have, effectively, the same ac polarizability. The two lasers are combined by a 50:50 beam splitter and coupled into a single-mode fiber, thereby enforcing the same spatial mode. Without changing the fluorescence signal size, which could contaminate the Stark-shift measurement by varying servo errors due to line-shape asymmetry and error-signal offsets, we vary the power of the detuned laser and measure the associated shift.

The results of this measurement are shown in Fig. 3 along with a linear regression used to determine the sensitivity coefficient $k(w_0)$. The measured fractional clock shift coefficient is $4.8(4) \times 10^{-13}$/mW for $w_0 = 0.66(5)$ μm. A previous measurement [28], appropriately scaled to match our beam radius, reported a coefficient of $4.5(4) \times 10^{-13}$/mW, which falls well within the error bars of the two measurements.

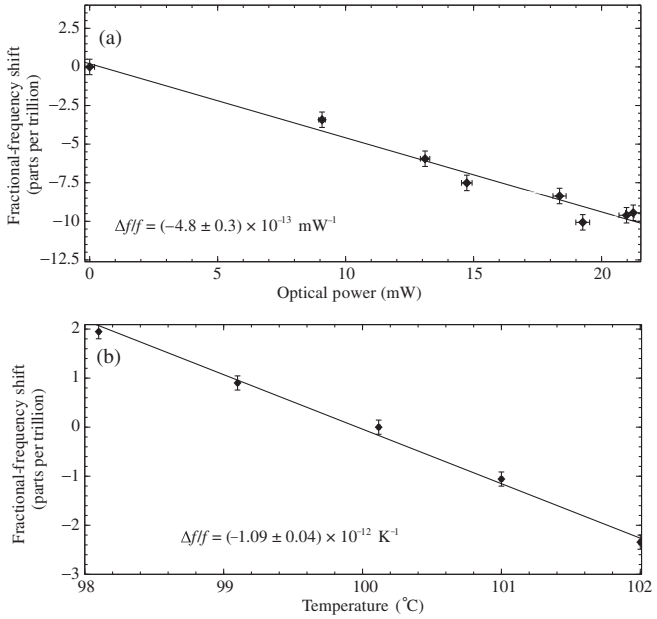

FIG. 3. (a) Experimentally measured 778-nm ac Stark shift for a (0.66 ± 0.05)-mm beam. The fitting routine employs orthogonal distance regression (ODR) to account for error bars in both coordinates, yielding a reduced χ^2 of 1.57. (b) Experimentally measured dependence of the clock frequency on vapor-cell temperature, again fit with ODR to yield a reduced χ^2 value of 0.908.

This coefficient indicates that the optical power must be stabilized to 2.1 μW to achieve 1×10^{-15} clock instability, requiring a precise laser power controller. A laser power stabilization circuit is constructed (Fig. 2) using feedback to a fiber-optic variable optical attenuator, which supports a loop bandwidth of 1 kHz. We find it most effective to use the fluorescence signal detected on the photomultiplier tube as the laser power sensor, rather than a sampled beam measured on a photodiode, although the latter is used as an out-of-loop witness sensor. This out-of-loop data are used to determine the fractional clock limitation imposed by laser power instability, as shown in Fig. 6.

C. Zeeman shift

Stray magnetic fields are an important environmental variable that can produce substantial atomic frequency shifts. The magnetic-field shift in the incomplete Paschen-Back regime of the $5S_{1/2}$ ground state can be analytically calculated utilizing the Breit-Rabi formula; because our spectroscopic technique does not resolve transitions between

specific magnetic sublevels, we then average over all relevant m_I and m_J magnetic quantum numbers.

This assumption results in no first-order (linear) dependence of the clock frequency on magnetic field, and it is valid for local magnetic fields $\lesssim$100 mG, which is roughly the field at which Zeeman-induced line broadening exceeds the natural linewidth of the two-photon transition. Substitution of the Landé g factors, g_J and g_I, and the magnetic dipole constant from Refs. [38,39] yields a second-order state shift of 114 Hz/G^2 for ^{87}Rb ($F = 2$) and 358 Hz/G^2 for ^{85}Rb ($F = 3$). The clock shift for the $5D_{5/2}$ excited state does not have a simple analytical solution. The Hamiltonian,

$$\begin{aligned}
\boldsymbol{H} &= \boldsymbol{H}_{\mathrm{hfs}} + \boldsymbol{H}_B^{(\mathrm{hfs})},\\
\boldsymbol{H}_{\mathrm{hfs}} &= A_{\mathrm{hfs}}\frac{\boldsymbol{I}\cdot\boldsymbol{J}}{\hbar^2}\\
&\quad + B_{\mathrm{hfs}}\frac{\frac{3}{\hbar^2}(\boldsymbol{I}\cdot\boldsymbol{J})^2 + \frac{3}{2\hbar}(\boldsymbol{I}\cdot\boldsymbol{J}) - J(J+1)I(I+1)}{2I(2I-1)J(2J-1)},\\
\boldsymbol{H}_B^{(\mathrm{hfs})} &= \mu_B(g_J\boldsymbol{J}_z + g_I\boldsymbol{I}_{\boldsymbol{Z}})B,
\end{aligned}$$

where $\boldsymbol{I}$ is the nuclear spin, $\boldsymbol{J}$ is the total angular momentum, μ_B is the Bohr magneton, and B is the applied magnetic field, is generated and diagonalized numerically.

Substituting the magnetic dipole and quadrapole constants, A_{hfs} and B_{hfs}, for the $5D_{5/2}$ level from Ref. [26] results in a state shift of 50 kHz/G^2 for ^{87}Rb ($F = 4$) and 190 kHz/G^2 for ^{85}Rb ($F = 5$). Expressing the differential Zeeman sensitivities in fractional-frequency units, we find the net clock shifts to be 6.5×10^{-11}/G^2 for ^{87}Rb and 2.5×10^{-10}/G^2 for ^{85}Rb. The energy-level splitting diagram for the exited state of ^{87}Rb is shown in Fig. 4.

With these coefficients, we can now specify the magnetic-shielding requirements; for ^{87}Rb (^{85}Rb), the magnetic field should be stable at the 3.9-mG (2.0-mG) level. We install a rectangular mu-metal shield 5 mm thick, for which the expected shielding factor exceeds 1000. In practice, the shielding factor is reduced due to openings for the heat pipes, optical fiber, electrical cabling, and photomultiplier tube, but we nonetheless expect the residual magnetic field at the vapor cell to be $\lesssim$1 mG.

D. Collisional shift

Collisions between two rubidium atoms can perturb the ground- and excited-state electronic wave functions, in principle leading to both a density-dependent collisional shift and a spectral line broadening. While exact details of these processes, which depend on the Rb-Rb molecular potentials, have not been published, Zameroski *et al.* [33] reported that line broadening is insignificant for this system as long as the vapor cell is operated below 125 °C, and the authors further reported a collisional shift coefficient in fractional frequency of 3.5×10^{-8}/Torr. Practically

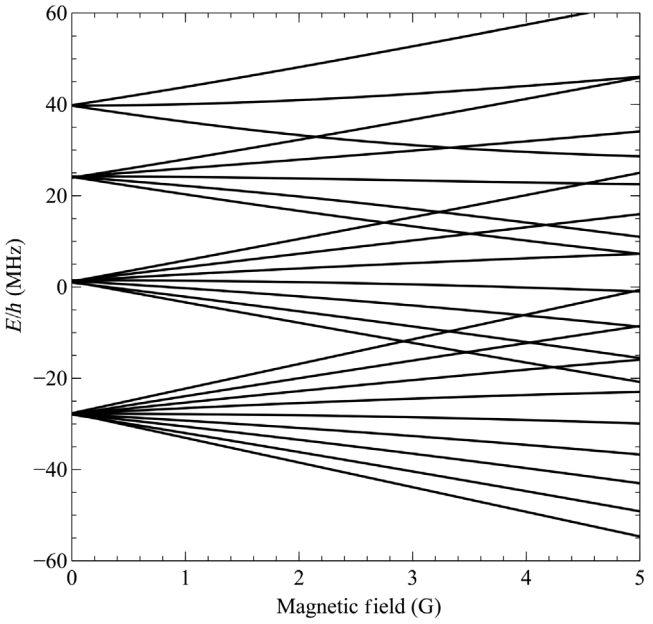

FIG. 4. Magnetic-field splitting for the $5D_{5/2}$ states of ^{87}Rb, which is determined by numerical diagonalization of the total Hamiltonian, as described in the text.

speaking, this coefficient places a tight constraint on the temperature stability of the coldest surface of the vapor cell, which effectively controls the saturated vapor density.

The vapor-cell temperature is determined using a standard 100-Ω resistive temperature detector (RTD) four-wire measurement, with a duplicate device for out-of-loop monitoring. Two independent temperature control stages are designed, a 333-K plate (temperature stage 1 in Fig. 2), to provide a stable reference temperature for heat-transfer control, and a second, more finely controlled 373-K stage (temperature stage 2), upon which the vapor cell is mounted (see Fig. 2). These stages are separated by four G-11 fiberglass posts to provide conductive thermal isolation. A precision temperature controller regulates a thermoelectric device and closes the temperature servo loops. Fiberglass insulation is added around the temperature control stages to reduce convective heat loss.

We measure a collisional shift for our ^{87}Rb-enriched vapor cell by varying the vapor-cell temperature. For each temperature change, the system is allowed to thermalize, whereupon the resulting frequency shift is measured over 300 s. The obtained frequency vs temperature is plotted in Fig. 3, and the fit supports a clock shift of $-1.09(4) \times 10^{-12}$/K, which is a factor of 2 larger than that reported for ^{85}Rb by Zameroski *et al.* [33] in a vapor cell with natural Rb. While this discrepancy could, in principle, be due to isotope-dependent collisional shift coefficients, it could also be due to noncollisional effects that are also varied when the cell temperature is changed, such as servo errors. Regardless, the measurement performed here accurately characterizes the system's sensitivity to vapor-cell temperature; at 373 K,

the temperature must be stable to 0.92 mK to achieve a fractional-frequency stability of 1×10^{-15}. The fractional clock limitation caused by the temperature fluctuations of temperature stage 2, measured by the out-of-loop RTD, is shown in Fig. 6.

E. Other considerations

A frequency-modulation technique utilizing a phase modulator is employed to lock the laser to the Rb $5S_{1/2} \rightarrow 5D_{5/2}$ two-photon transition. This technique is known to suffer from residual amplitude modulation (RAM) that arises when modulation sidebands are not equal in magnitude or opposite in phase [40,41]. Zhang *et al.* developed a technique to suppress both in-phase and quadrature RAM [42] utilizing a feedback control of the phase modulator's dc bias and temperature, respectively. We employ a similar technique using a single feedback loop to the dc bias voltage, supporting a loop bandwidth of 10 kHz, which is combined with a sinusoidal modulation signal on a bias tee, as shown in Fig. 2. This method yields suppression of > 35 dB. Additionally, we find benefit in saturating the input to the 1556-nm optical amplifier, which provides a passive reduction of RAM of > 5 dB. While these two suppression mechanisms are sufficient to achieve the fractional clock instabilities shown in Fig. 6, it may be necessary to apply corrections to quadrature RAM by stabilizing the temperature of the EOM to further decrease the clock instabilities.

Doppler effects are largely eliminated by retroreflecting the laser beam that passes through the vapor cell. However, residual broadening related to the absorption of two photons from the same beam remains; this contribution to the line shape is a Gaussian function with a full width at half maximum of $\sqrt{8k_BT \ln 2/mc^2}\nu_0 \approx 571$ MHz for ^{87}Rb at $T = 373$ K, with k_B being the Boltzmann constant and m the atomic mass. Absorbing two photons from the same beam occurs with the same probability as absorbing one photon from each beam; however, the linewidth associated with the former process is 1000 times greater than the latter. Hence, the Doppler-broadened peak is not easily resolved, and residual Doppler effects are small.

The significant tails of the Lorentzian peaks of neighboring hyperfine transitions pull the spectral lines closer together, a phenomenon known as line pulling. The amount by which a particular transition is shifted is calculated by summing over all relevant hyperfine Lorentzians, with the appropriate frequencies and strengths given by Ref. [26]. The two-photon transition is shifted by 0.477 Hz for ^{85}Rb and 0.030 Hz for ^{87}Rb. This calculation does not take into account possible cross-damping terms, which can arise from quantum interference between multiple decay paths associated with neighboring, off-resonant transitions [43].

Second-order Doppler broadening, taking into account first-order relativistic corrections, is given by

$$\frac{\delta\omega}{\omega} = \frac{\bar{v}^2}{2c^2}, \tag{4}$$

where $\bar{v}^2 = 8k_bT/m\pi$. For Rb at 373 K, the fractional clock shift is 5×10^{-13} with a slope of 10^{-15}/K.

The atomic vapor is immersed in a bath of electromagnetic radiation whose spectrum follows Planck's law. In many cases, the blackbody radiation (BBR) shift can be treated as a dc Stark shift since the radiation is far off resonance from all relevant atomic transitions [44]. However, the operational temperature of our system, 373 K, yields a blackbody spectrum that is nearly resonant with several transitions connecting to the $5D_{5/2}$ state. Farley and Wing derived this perturbation for hydrogen, helium, and the alkali-metal atoms for electromagnetic radiation at 300 K [45]. Hilico *et al.*, calculated, assuming a T^4 behavior, that the perturbation would yield a shift of -210 Hz with a local slope of approximately 1 Hz/K [28] at 373 K. The fractional clock shift arising from BBR is 1.3×10^{-15}/K, requiring that the blackbody source be held to temperatures more stable than 770 mK; however, atomic Rb transitions near resonance with the blackbody spectrum at 373 K possibly impact the accuracy of this estimate.

The dc polarizability of the $5D_{5/2}$ state is measured in Ref. [46], and it exceeds that of the $5S_{1/2}$ state by a factor of about 50 due to low-lying transitions to nearby levels. Using this polarizability, we calculate the fractional clock sensitivity to dc electric fields as $5.9 \times 10^{-15}/(\mathrm{V/cm})^2$. The magnetic shield surrounding the vapor-cell assembly also acts as a Faraday cage to prevent external electric fields from reaching the atomic vapor. However, stray charge could accumulate on the glass vapor cell itself; any resulting patch potentials need to be stable at the 0.5-V level.

Experimentally determined collisional shifts in Ref. [33] for various noble gases are examined to put limits on vapor-cell impurities. Helium is the only gas known to permeate the vapor cell, and it produces frequency shifts of -2.1 MHz/Torr. Therefore, we obtain that a helium leak rate of $< 3.6 \times 10^{-8}$ Torr/day must be achieved in order to achieve fractional clock instabilities below 1×10^{-15}. The cell may also be permeable to methane, which has an atmospheric composition of about 3 times less than helium, but the shift rate due to methane has not yet been measured, to our knowledge.

IV. RESULTS

Having assessed the leading contributions to instability, we next measure the clock performance by photodetecting the comb repetition rate and counting it relative to a hydrogen maser. During data collection, the vapor-cell temperature and 778-nm laser power are monitored. The counter is gated at a rate of 1 Hz, and the resulting frequency record is analyzed after removing a linear drift of -1×10^{-18}/s. Figure 5 shows the resulting total Allan deviation for a time record of 40 000 s, and the system is

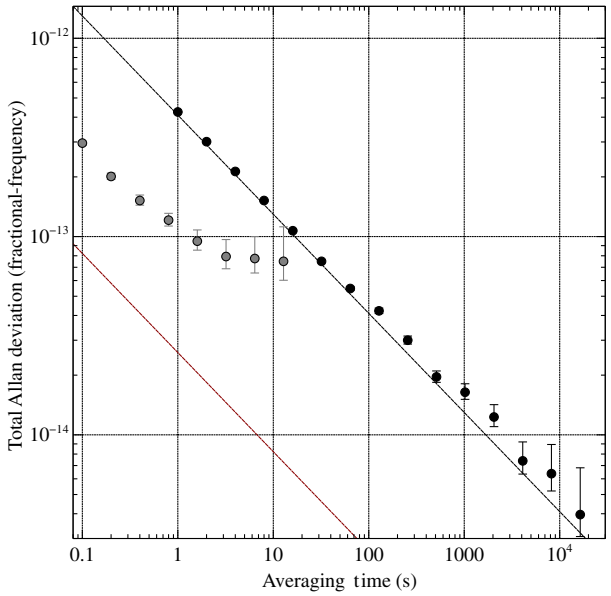

FIG. 5. The measured fractional-frequency instability for typical operating conditions (the black circles) plotted as a total Allan deviation along with a $1/\sqrt{\tau}$ white-noise line (the black solid line). Also shown are the measured instability when the frequency standard is operated with a larger signal-to-noise ratio (the gray circles) and the expected intermodulation limit (the red line), as described in Sec. III A.

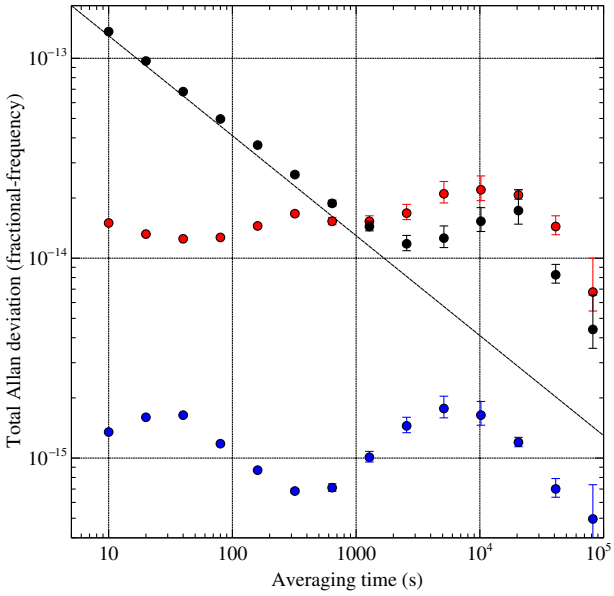

FIG. 6. The fractional-frequency instability plotted as a total Allan deviation for ^{87}Rb with $1/\sqrt{\tau}$ white noise (black), as well as anticipated limits on the clock stability arising from cell temperature fluctuations (blue) and laser power fluctuations (red). We believe the instability limit arising from laser power fluctuations is an overestimate due to temperature-dependent effects in the witness photodiode, as described in the text.

shown to average $4 \times 10^{-13}/\sqrt{\tau(s)}$ for τ values from 1 to 10 000 s. On longer time scales, however, we find that the instability increases. Figure 6 shows the total Allan deviation for a record of 180 000 s, as well as the expected clock performance limitations derived from out-of-loop measurements of the cell temperature and the laser power. On some time scales, the clock performance exceeds the expected stability as determined from laser power measurements; however, long-term laser power measurements from the witness photodiode are thought to be particularly influenced by room-temperature fluctuations, and these temperature variations may lead to an overestimation of Stark shift-related clock instability. The apparent "bump" in all signals around 10^4 s is likely caused by room-temperature fluctuations, indicating that the frequency standard performance can be improved by more tightly regulating the system temperature.

V. CONCLUSIONS AND FUTURE OUTLOOK

In this paper, we demonstrate that our system is capable of averaging down less than 7×10^{-15} at 16 000 s and to $\lesssim 1 \times 10^{-14}$ at 1 day. It appears that, on time scales beyond a few hours, the instability is related to the ac Stark shift, which would indicate that an improved method for detecting and stabilizing the laser power will be required to achieve fractional-frequency instabilities of 1×10^{-15} at 1 day. The initial optical design of the vapor-cell assembly implements a photodiode, thermally anchored to temperature stage 2 for reduction of temperature-influenced drifts, as the in-loop laser power sensor. We instead implement the PMT photocurrent as the feedback sensor because we find that it produces superior results. One advantage of stabilizing the laser power based on the detected fluorescence signals is that it relies on an atomic signal rather than a beam sampling optic, for which the reflectivity is subject to polarization and temperature variations. Nevertheless, thermal considerations are still required, as the PMT's conversion efficiency is also temperature dependent [47], with an expected coefficient of 0.5% to 1% per kelvin. Within the current design of the vapor-cell assembly, an attempt is made to thermally connect the PMT to temperature stage 2, and fiberglass insulation is used to reduce thermal parasitics. However, temperature gradients are difficult to minimize over the 10-cm length of the PMT. Additionally, the PMT's high-voltage power supply and transimpedance amplifier need to provide constant voltage and gain, respectively, in order to use the PMT as a long-term laser power sensor.

Alternatively, if improving the laser power stability proves too challenging, there are several design modifications that allow the two-photon clock to operate with a smaller ac Stark shift. First, the spectral linewidth can be decreased by removing the helium contamination in the vapor cell; in our current cells, which are expected to be saturated with 4 mTorr of helium, the linewidth is

approximately a factor of 2 larger than the natural linewidth. Removing the helium (through the use of a vacuum chamber or a helium-resistant cell [48]) would allow for a reduced laser power by a factor of 2 without affecting the short-term stability. Additional modifications include increasing the efficiency of the fluorescence detection, increasing the effective length of the vapor cell by routing the beam through the vapor on multiple, nonoverlapping passes, increasing the vapor density, and decreasing the desired short-term stability metric. Another final option is to increase the laser beam radius and laser power together; increasing both the power P and the intensity radius w_0 by a factor of F results in the same photon detection rate (accounting for both the decreased optical intensity and the increased number of atoms in the beam path) but a smaller overall ac Stark shift by the same factor F.

Beyond improvements to the stability, future work with this system necessarily involves miniaturizing and hardening the laser and frequency comb for future field deployment. Particular emphasis will need to be paid to automation of the locking electronics and simplification of the control loop architecture, which currently includes ten independent temperature control segments. Reducing the power consumption of the frequency comb, which currently uses four pump lasers, is another important area of research. Finally, any attempt to prepare this type of advanced optical clock for space will have to overcome the challenge of radiation-induced darkening of the optical components. Despite these challenges, we remain optimistic that a vapor-cell optical clock, such as the one described here, could soon be deployed to provide precise timekeeping for a host of applications.

ACKNOWLEDGMENTS

We thank Jordan Armstrong and the Space Dynamics Laboratory machine shop for assistance in constructing the experimental apparatus. We thank Steve Lipson for his careful reading of the manuscript. Contributions to this article by workers at AFRL, an agency of the U.S. Government, are not subject to U.S. copyright.

[1] L. Maleki and J. Prestage, Applications of clocks and frequency standards: From the routine to tests of fundamental models, Metrologia **42**, S145 (2005).

[2] R. Wynands and S. Weyers, Atomic fountain clocks, Metrologia **42**, S64 (2005).

[3] T. E. Parker, S. R. Jefferts, T. P. Heavner, and E. A. Donley, Operation of the NIST-F1 caesium fountain primary frequency standard with a maser ensemble, including the impact of frequency transfer noise, Metrologia **42**, 423 (2005).

[4] J. Guena, M. Abgrall, D. Rovera, P. Laurent, B. Chupin, M. Lours, G. Santarelli, P. Rosenbusch, M. E. Tobar, R. Li, K. Gibble, A. Clairon, and S. Bize, Progress in atomic fountains at LNE-SYRTE, IEEE Trans. Ultrason. Ferroelectr. Freq. Control **59**, 391 (2012).

[5] J. G. McNeff, The global positioning system, IEEE Trans. Microwave Theory Tech. **50**, 645 (2002).

[6] V. Formichella, J. Camparo, and P. Travella, Influence of the ac-Stark shift on GPS atomic clock timekeeping, Appl. Phys. Lett. **110**, 043506 (2017).

[7] Peter Yun, François Tricot, Claudio Eligio Calosso, Salvatore Micalizio, Bruno François, Rodolphe Boudot, Stéphane Guérandel, and Emeric de Clercq, High-Performance Coherent Population Trapping Clock with Polarization Modulation, Phys. Rev. Applied **7**, 014018 (2017).

[8] A. Godone, F. Levi, C. E. Calosso, and S. Micalizio, High-performing vapor-cell frequency standards, Riv. Nuovo Cimento **38**, 133 (2015).

[9] S. Micalizio, C. E. Calosso, A. Godone, and F. Levi, Metrological characterization of the pulsed Rb clock with optical detection, Metrologia **49**, 425 (2012).

[10] Liang Liu *et al.*, Test of cold atom clock in orbit, arXiv:1709.03256.

[11] D. J. Jones, S. A. Diddams, J. K. Ranka, A. Stentz, R. S. Windeler, J. L. Hall, and S. T. Cundiff, Carrier-envelope phase control of femtosecond mode-locked lasers and direct optical frequency synthesis, Science **288**, 635 (2000).

[12] S. A. Diddams, D. J. Jones, J. Ye, S. T. Cundiff, J. L. Hall, J. K. Ranka, R. S. Windeler, R. Holzwarth, T. Udem, and T. W. Hansch, Direct Link between Microwave and Optical Frequencies with a 300 THz Femtosecond Laser Comb, Phys. Rev. Lett. **84**, 5102 (2000).

[13] R. Holzwarth, T. Udem, T. W. Hansch, J. C. Knight, W. J. Wadsworth, and P. S. J. Russell, Optical Frequency Synthesizer for Precision Spectroscopy, Phys. Rev. Lett. **85**, 2264 (2000).

[14] N. Hinkley, J. A. Sherman, N. B. Phillips, M. Schioppo, N. D. Lemke, K. Beloy, M. Pizzocaro, C. W. Oates, and A. D. Ludlow, An atomic clock with 10^{-18} instability, Science **341**, 1215 (2013).

[15] B. J. Bloom, T. L. Nicholson, J. R. Williams, S. L. Campbell, M. Bishof, X. Zhang, W. Zhang, S. L. Bromley, and J. Ye, An optical lattice clock with accuracy and stability at the 10^{-18} level, Nature (London) **506**, 71 (2014).

[16] T. L. Nicholson, S. L. Campbell, R. B. Hutson, G. E. Marti, B. J. Bloom, R. L. McNally, W. Zhang, M. D. Barrett, M. S. Safronova, G. F. Strouse, W. L. Tew, and J. Ye, Systematic evaluation of an atomic clock at 2×10^{-18} total uncertainty, Nat. Commun. **6**, 6896 (2015).

[17] N. Huntemann, C. Sanner, B. Lipphardt, Chr. Tamm, and E. Peik, Single-Ion Atomic Clock with 3×10^{-18} Systematic Uncertainty, Phys. Rev. Lett. **116**, 063001 (2016).

[18] C. W. Chou, D. B. Hume, J. C. J. Koelemeij, D. J. Wineland, and T. Rosenband, Frequency Comparison of Two High-Accuracy Al^+ Optical Clocks, Phys. Rev. Lett. **104**, 070802 (2010).

[19] S. B. Koller, J. Grotti, St. Vogt, A. Al-Masoudi, S. Dörscher, S. Häfner, U. Sterr, and Ch. Lisdat, Transportable Optical Lattice Clock with 7×10^{-17} Uncertainty, Phys. Rev. Lett. **118**, 073601 (2017).

[20] Thilo Schuldt, Klaus Döringshoff, Evgeny V. Kovalchuk, Anja Keetman, Julia Pahl, Achim Peters, and Claus Braxmaier, Development of a compact optical absolute

frequency reference for space with 10^{-15} instability, Appl. Opt. **56**, 1101 (2017).
[21] J. Lodewyck, S. Bilicki, E. Bookjans, J. Robyr, C. Shi, G. Vallet, R. Le Targat, D. Nicolodi, Yann Le Coq, J. Guéna, M. Abgrall, P. Rosenbusch, and S. Bize, Optical to microwave clock frequency ratios with a nearly continuous strontium optical lattice clock, Metrologia **53**, 1123 (2016).
[22] I. R. Hill, R. Hobson, W. Bowden, E. M. Bridge, S. Donnellan, E. A. Curtis, and P. Gill, J. Phys. Conf. Ser. **723**, 012019 (2016).
[23] Matthias Lezius *et al.*, Space-borne frequency comb metrology, Optica **3**, 1381 (2016).
[24] L. C. Sinclair, J.-D. Deschnes, L. Sonderhouse, W. C. Swann, I. H. Khader, E. Baumann, N. R. Newbury, and I. Coddington, Invited article: A compact optically coherent fiber frequency comb, Rev. Sci. Instrum. **86**, 081301 (2015).
[25] G. Grynberg and B. Cagnac, Doppler-free multiphotonic spectroscopy, Rep. Prog. Phys. **40**, 791 (1977).
[26] F. Nez, F. Biraben, R. Felder, and Y. Millerioux, Optical frequency determination of the hyperfine components of the $5S_{1/2} \rightarrow 5D_{5/2}$ two-photon transitions in rubidium, Opt. Commun. **102**, 432 (1993).
[27] D. Touahri, O. Acef, A. Clairon, J.-J. Zondy, R. Felder, L. Hilico, B. de Beauvoir, F. Biraben, and F. Nez, Frequency measurement of the $5S_{1/2}(f = 3) \rightarrow 5D_{5/2}(f = 5)$ two-photon transition in rubidium, Opt. Commun. **133**, 471 (1997).
[28] L. Hilico, R. Felder, D. Touahri, O. Acef, A. Clairon, and F. Biraben, Metrological features of the rubidium two-photon standards of the BNM-LPTF and Kastler Brossel Laboratories, Eur. Phys. J. Appl. Phys. **4**, 219 (1998).
[29] N. Kuse, C.-C. Lee, J. Jiang, C. Mohr, T. R. Schibli, and M. E. Fermann, Ultra-low noise all polarization-maintaining Er fiber-based optical frequency combs facilitated with a graphene modulator, Opt. Express **23**, 24342 (2015).
[30] Adela Marian, Matthew C. Stowe, John R. Lawall, Daniel Felinto, and Jun Ye, United time-frequency spectroscopy for dynamics and global structure, Science **306**, 2063 (2004).
[31] Jiutao Wu, Dong Hou, Zhengyu Qin, Zhigang Zhang, and Jianye Zhao, Observation of Rb two-photon absorption directly excited by an erbium-fiber-laser-based optical frequency comb via spectral control, Phys. Rev. A **89**, 041402 (2014).
[32] K. D. Rathod and V. Natarajan, Accessing the $5S_{1/2} \rightarrow 5D_{5/2}$ two-photon transition in Rb using a diode laser system, Sci. Culture **83**, 39 (2017).
[33] Nathan D. Zameroski, Gordon D. Hager, Christopher J. Erickson, and John H. Burke, Pressure broadening and frequency shift of the $5S_{1/2} \rightarrow 5D_{5/2}$ and $5S_{1/2} \rightarrow 7S_{1/2}$ two photon transitions in ^{85}Rb by the noble gases and N_2, J. Phys. B **47**, 225205 (2014).
[34] P. J. Oreto, Y.-Y. Jau, A. B. Post, N. N. Kuzma, and W. Happer, Buffer-gas-induced shift and broadening of hyperfine resonances in alkali-metal vapors, Phys. Rev. A **69**, 042716 (2004).
[35] J. J. Snyder, Paraxial ray analysis of a cat's-eye retroreflector, Appl. Opt. **14**, 1825 (1975).
[36] C. Audoin, V. Candelier, and N. Dimarcq, in *Proceedings of the Conference on Precision Electromagnetic Measurements (CPEM '90), Ottawa, 1990* (IEEE, New York, 1990), p. 93.
[37] G. J. Dick, in *Proceedings of the Nineteenth Annual Precise Time and Time Interval (PTTI) Applications and Planning Meeting, Redondo Beach, CA, 1987*, p. 133.
[38] E. Arimondo, M. Inguscio, and P. Violino, Experimental determinations of the hyperfine structure in the alkali atoms, Rev. Mod. Phys. **49**, 31 (1977).
[39] S. Bize, Y. Sortais, M. S. Santos, C. Mandache, A. Clairon, and C. Salomon, High-accuracy measurement of the ^{87}Rb ground-state hyperfine splitting in an atomic fountain, Europhys. Lett. **45**, 558 (1999).
[40] G. C. Bjorklund, Frequency-modulation spectroscopy: A new method for measuring weak absorptions and dispersions, Opt. Lett. **5**, 15 (1980).
[41] Jun Ye, Long-Sheng Ma, and John L. Hall, Ultrasensitive detections in atomic and molecular physics: Demonstration in molecular overtone spectroscopy, Opt. Lett. **15**, 6 (1998).
[42] W. Zhang, M. J. Martin, C. Benko, J. L. Hall, J. Ye, C. Hagemann, T. Legero, U. Sterr, F. Riehle, G. D. Cole, and M. Aspelmeyer, Reduction of residual amplitude modulation to 1×10^{-6} for frequency modulation and laser stabilization, Opt. Lett. **39**, 1980 (2014).
[43] D. C. Yost, A. Matveev, E. Peters, A. Beyer, T. W. Hänsch, and Th. Udem, Quantum interference in two-photon frequency-comb spectroscopy, Phys. Rev. A **90**, 012512 (2014).
[44] Wayne M. Itano, L. L. Lewis, and D. J. Wineland, Shift of $^2S_{1/2}$ hyperfine splittings due to blackbody radiation, Phys. Rev. A **25**, 1233 (1982).
[45] John W. Farley and William H. Wing, Accurate calculation of dynamic stark shifts and depopulation rates of Rydberg energy levels induced by blackbody radiation. Hydrogen, helium, and alkali-metal atoms, Phys. Rev. A **23**, 2397 (1981).
[46] D. Tregubov, S. Snigirev, A. Golovizin, S. Pyatchenkov, D. Sukachev, A. Akimov, V. Sorokin, and N. Kolachevskyv, Measurement of the $5D$ level polarizabilities in laser cooled Rb atoms, J. Phys. Conf. Ser. **635**, 092121 (2015).
[47] A. T. Young, Temperature effects in photomultipliers and astronomical photometry, Appl. Opt. **2**, 51 (1963).
[48] Argyrios T. Dellis, Vishal Shah, Elizabeth A. Donley, Svenja Knappe, and John Kitching, Low helium permeation cells for atomic microsystems technology, Opt. Lett. **41**, 2775 (2016).